Fast photon-mediated entanglement of continuously-cooled trapped ions for quantum networking

Jameson O'Reilly,[1,*] George Toh,[1] Isabella Goetting,[1] Sagnik Saha,[1] Mikhail Shalaev,[1] Allison Carter,[2,†] Andrew Risinger,[2,‡] Ashish Kalakuntla,[1] Tingguang Li,[1] Ashrit Verma,[1] and Christopher Monroe[1,2]

[1]*Duke Quantum Center, Departments of Electrical and Computer Engineering and Physics, Duke University, Durham, NC 27708*

[2]*Joint Quantum Institute, Departments of Physics and Electrical and Computer Engineering, University of Maryland, College Park, MD 20742*

(Dated: April 26, 2024)

We entangle two co-trapped atomic barium ion qubits by collecting single visible photons from each ion through in-*vacuo* 0.8 NA objectives, interfering them through an integrated fiber-beamsplitter and detecting them in coincidence. This projects the qubits into an entangled Bell state with an observed fidelity lower bound of $F > 94\%$. We also introduce an ytterbium ion for sympathetic cooling to remove the need for recooling interruptions and achieve a continuous entanglement rate of 250 s^{-1}.

Photonic interconnects between quantum processing nodes may be the only way to achieve large-scale quantum computers, and such an architecture has been proposed for the leading qubit platforms [1–4]. Using these connections to distribute remote entanglement between computing modules with high rates and near-unit fidelity should enable universal and fully-connected control over a substantially larger Hilbert space, greatly increasing the collective power of the quantum processors [5–7]. Interconnects between quantum memories, even without multi-qubit universal control, also offer diverse opportunities in quantum sensing [8, 9], communication [10], and quantum simulation.

Trapped ions are attractive candidates for both quantum computing and networking due to their natural homogeneity, isolation from their environment, and indefinite idle coherence times [11]. These advantages, along with decades of technological development, have led to demonstrations of the highest-fidelity state preparation and measurement (SPAM) [12] and coherent operations [13–15], all performed in small systems of just one or two ions. Low errors have also been achieved in medium-sized chains [16, 17], with limits due to weaker trap confinement and resulting motional mode-crowding and crosstalk concerns. Alternatively, smaller ion chains can be shuttled between interaction zones [18, 19], but transport already dominates the time budget of current systems with up to 32 qubits [20].

Photonic interconnects can avoid the overhead associated with controlling larger chains and finite shuttling speeds, but they rely on probabilistic excitation and photon emission protocols and finite photon collection efficiencies. The current state-of-the-art photon-mediated entangling rate between trapped ion qubits is 182 s^{-1} [21], on par with the mean entanglement rate in shuttling architectures [20] but much slower than typical local entangling rates of 10-100 kHz [22, 23]. This demonstration was mainly limited by a success probability of 2.18×10^{-4} in each attempt [21] where the leading inefficiency is the use of 0.6 numerical aperture (NA) objectives that only collect 10% of the photons from each ion. A higher success probability of 2.9×10^{-4} has been achieved by surrounding ions with optical cavities, but the requirement of a much lower attempt rate led to a success rate of just 0.43 s^{-1} [24]. In these experiments, the attempt rate is limited by initialization steps, including periodic interruptions to recool the ions, as heating from photon recoil can reduce the collection efficiency and cause state measurement errors [25].

In this work, we utilize two 0.8 NA objectives to demonstrate photon-mediated entanglement between $^{138}Ba^+$ ions with a success probability of $2.33(5) \times 10^{-4}$ and a fidelity $F \geq 93.7(1.3)\%$. Then, we introduce $^{171}Yb^+$ as a sympathetic coolant to achieve an uninterrupted attempt rate of 1 MHz and an ion-ion qubit entanglement rate of 250(8) s^{-1}. We choose to work with $^{138}Ba^+$because it offers the longest-wavelength $S-P$ dipole transition of the commonly-trapped ion species at 493 nm and is similar in mass to $^{171}Yb^+$, a well-established species for quantum computing [16, 17, 20]. Photons at 493 nm can also be converted to telecom wavelengths for long-distance networking [28].

We begin by trapping two $^{138}Ba^+$ ions in a four-rod rf Paul trap and Doppler-cooling them with 493 and 650 nm light. Two 0.8 NA in-*vacuo* objectives [26] collect the ion fluorescence with each lens aligned to a different ion and no measurable crosstalk after coupling into single-mode optical fibers (see Figure 1). To generate entanglement between each ion and its emitted photon, we begin by optically pumping each $^{138}Ba^+$ion

* Corresponding author: jameson.oreilly@duke.edu

† Present Address: National Institute of Standards and Technology, Boulder CO 80305

‡ Present Address: Intel Corp., Hillsboro, OR 97124

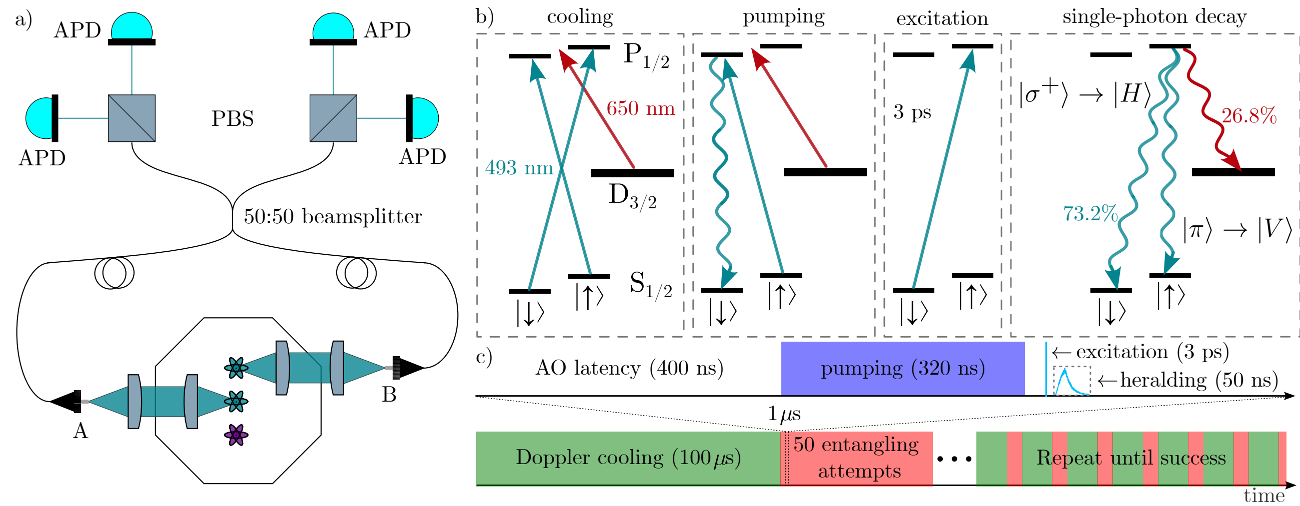

Figure 1. Overview of the experiment. (a) Three co-trapped ions with two barium ions imaged by in-*vacuo* 0.8 NA objectives [26] and an optional ytterbium ion for sympathetic cooling. Scattered light at 493 nm is coupled into single mode optical fibers and routed to a Bell state analyzer consisting of an in-fiber beamsplitter to erase which-path information and polarizers to measure the photon state [27]. (b) $^{138}Ba^+$ level diagrams for each operation associated with ion-photon entanglement generation. Our qubit states are defined as $|\downarrow\rangle \equiv |S_{1/2}, m_J = -1/2\rangle$ and $|\uparrow\rangle \equiv |S_{1/2}, m_J = +1/2\rangle$. (c) Timeline for entanglement generation attempts without sympathetic cooling. Each 1 μs-long attempt consists of optical pumping, pulsed excitation, single photon collection, and fast logic to check for a heralding detection pattern. If no such pattern occurs, we repeat attempts up to 50 times before breaking for Dopper cooling. After cooling, we repeat this cycle until success.

to $|\downarrow\rangle \equiv |S_{1/2}, m_J = -1/2\rangle$ and then exciting to $|P_{1/2}, m_J = +1/2\rangle$ with near-unit probability using a 3 ps pulse of σ^+ 493 nm light. When the ion returns to the $S_{1/2}$ state after spontaneous emission (lifetime $\sim$ 8 ns), it can decay to either $|\downarrow\rangle$ or $|\uparrow\rangle \equiv |S_{1/2}, m_J = +1/2\rangle$, correlated with the photon polarization. When a 493 nm photon is collected perpendicular to the magnetic field axis and coupled into a single-mode fiber, the photon and its parent ion are projected to the state

$$\frac{|H\rangle\,|\downarrow\rangle + |V\rangle\,|\uparrow\rangle}{\sqrt{2}}, \tag{1}$$

where $|H\rangle$ and $|V\rangle$ represent orthogonal polarizations. The static phase of the above superposition is set to zero for convenience and without loss of generality.

To show ion-photon correlations from either source, we integrate for 50 ns following the excitation pulse, and if a single photon is detected, we proceed to state analysis and detection. Otherwise, we either repeat the attempt or break for 100 μs of Doppler cooling after 50 successive attempts, for a duty cycle of 33%. Each attempt takes 1 μs, dominated by AOM latency and state preparation, and has independent single-photon success probabilities of $\eta_A = 2.3(1)\%$ and $\eta_B = 2.2(1)\%$ (see Supplemental Material) through each of the two ion imaging systems (hereafter labelled A and B).

After the photon exits the fiber, it passes through a quarter-wave plate to compensate for any ellipticity. Then, we examine the ion-photon correlations by scanning the angle of a half-wave plate in the beam path and measuring both the photon polarization and the parent ion qubit state (Figs. 2a,c). The qubit is measured by shelving population in state $|\downarrow\rangle$ to the metastable $D_{5/2}$ manifold with 1762 nm light and then detecting the presence or absence of fluorescence under 493 and 650 nm illumination [29, 30], resulting in an estimated ion qubit detection fidelity of $\sim$ 99.5%. The resulting contrast in the correlation sets an upper bound on the fidelity overlap with Eq. 1 of $F_A < 99.1(1)\%$ and $F_B < 99.1(7)\%$, which we attribute to residual polarization mixing in the imaging systems.

To establish a lower bound for the fidelity of each ion-photon pair, we rotate each half wave plate by 45° so that single photon detections herald each parent ion into the equal superposition states

$$\frac{|\downarrow\rangle_j \pm e^{i\phi_j}\,|\uparrow\rangle_j}{\sqrt{2}}, \tag{2}$$

where the sign depends on which detector the photon hits and the phase ϕ_j $(j = A, B)$ is given by static polarization rotations in the fiber. Then, we use a pair of 532 nm Raman beams to drive a $\pi/2$ rotation of the atomic qubit with variable phase (Figs. 2b,d) [31]. The contrast of the qubit state population with this phase sets a lower bound on the ion-photon fidelities of $F_A > 98.1(1.4)\%$ and $F_B > 96.8(6)\%$ [32]. We also measure unmatched superposition phases of $\phi_A = 5.00(2)$ rad and $\phi_B = 0.48(2)$ rad caused by different uncompensated birefringence along the two photon paths.

Based on the measured qubit coherence time of $T_2^* =$

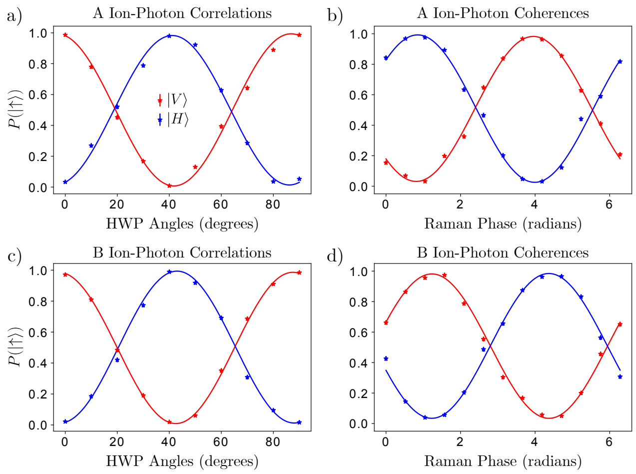

Figure 2. Characterization of ion-photon entanglement with the two single ion imaging systems. Statistical error bars are too small to be visible. Red and blue data points correspond to the probability that the ion is in the bright $|\uparrow\rangle$ state after a photon is detected in the V or H output mode of a polarizer. The solid lines are fits to sinusoidal functions.

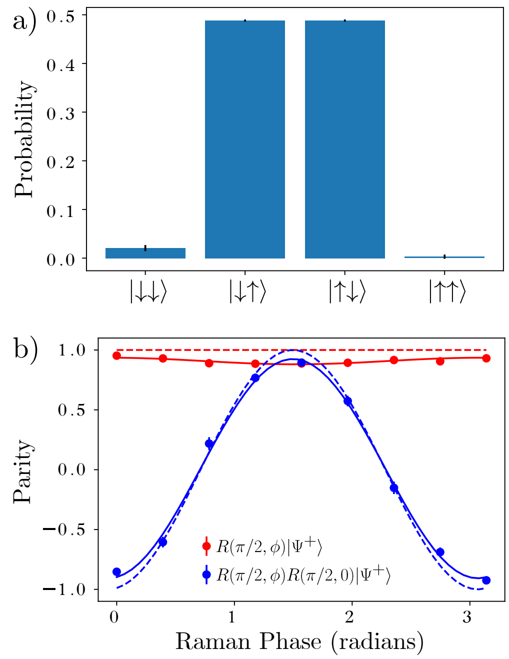

Figure 3. Ion-ion entanglement fidelity estimation. (a) Two-ion state based on fluorescence thresholding techniques described in the Supplemental Material (SM). Our method cannot distinguish between $|\downarrow\uparrow\rangle$ and $|\uparrow\downarrow\rangle$ but we assume here that they contribute equally to the measured one-bright population. (b) Parity scan for bounding the off-diagonal elements of the ion-ion state. The red data correspond to scanning the phase of a single $\pi/2$ pulse. The corresponding solid line is the fit and the dashed line represents the expected behavior of the ideal state $|\Psi^+\rangle$. The blue data correspond to scanning the phase of a second $\pi/2$ pulse after a $\pi/2$ pulse with fixed phase $\phi = 0$.

550(27) μs, limited by magnetic field fluctuations, we attribute 0.26(3)% of each infidelity to decoherence during the 40 μs before the analysis $\pi/2$ pulse. Another 0.10(2)% is due to averaging over different Raman phases in a reduced photon detection window of 3 ns. We bound errors from double excitations, crosstalk between the imaging systems, and excitation laser background to the 10^{-5} level by measuring the ratio between one and two photon events.

Having established ion-photon entanglement through each imaging system, we can now entangle the two ions by sending the photons into a Bell state analyzer as shown in Figure 1, thereby performing entanglement swapping. An in-fiber 50:50 beamsplitter erases the "which-path" information, so if we detect one H and one V photon in the same trial the ions are ideally heralded into the entangled state

$$\frac{|\downarrow\rangle_A\,|\uparrow\rangle_B \pm e^{i(\delta t+\phi)}\,|\uparrow\rangle_A\,|\downarrow\rangle_B}{\sqrt{2}}. \quad (3)$$

Here, the sign is determined by whether a coincident detection occurred on the same or opposite sides of the beamsplitter [27], $\delta \equiv \omega_B - \omega_A = 2\pi \times 984(2)$ Hz is the qubit frequency difference between the ions, t is the time elapsed after coincidence detection, and $\phi \equiv \phi_B - \phi_A$. This state suppresses the effect of common-mode noise [33, 34] and we indeed measure an extended Bell state coherence time of $T_2^* = 38(13)$ ms.

For this experiment, we measure the probability to generate one of the above maximally-entangled states to be $2.33(5) \times 10^{-4}$, which is consistent with the product of the measured ion-photon efficiencies above: $\frac{1}{2}\eta_A\eta_B = 2.50(16) \times 10^{-4}$, with the factor of 1/2 stemming from heralding only two of the four Bell states. The effective attempt rate of 333 kHz is the same as in the individual ion-photon measurements above, so the ion-ion entanglement rate is 78(2) s^{-1}.

We measure both the populations and coherences of the heralded state of the ions by applying appropriate qubit rotations to both ions, as described in the Supplemental Material. We measure the populations of the odd parity states to be $P_{\downarrow\uparrow} + P_{\uparrow\downarrow} = 97.6(5)\%$ with coherences $2\mathrm{Re}\left(\rho_{\downarrow\uparrow,\uparrow\downarrow} + \rho_{\downarrow\downarrow,\uparrow\uparrow}\right) = 92.5(1.7)\%$ [35, 36]. Bounding the other possible coherence terms results in a SPAM-corrected fidelity with respect to Eq. 3 of $F \geq 93.7(1.3)\%$ [37].

Based on the measured finite contrast of the spin-polarization correlations, we expect an infidelity of 2.9(1.6)%, which is consistent with the measured populations. The extended two-qubit coherence is expected to contribute 0.3(1)% and other sources including temporal mismatch and dark counts account for another 0.4(1)%. The total predicted infidelity of 3.6(1.6)% is thus within error of our measured infidelity. Notably, using an in-fiber beamsplitter avoids the percent-level error induced by imperfect free-space photon spatial mode overlap in prior experiments [21, 38].

Over the course of many consecutive entanglement generation attempts, recoil from optical pumping and pulsed excitation heats the ions, reducing the heralded success probability, as shown in Figure 4(b). Above, we capped the number of attempts without cooling at 50 to avoid this decay and to maintain high-fidelity state detection. We avoid these issues while maximizing the entanglement attempt rate by co-trapping a $^{171}\mathrm{Yb}^+$ ion for continuous sympathetic cooling.

We Doppler cool the $^{171}\mathrm{Yb}^+$ ion using 370 and 935 nm light, with sufficient spectral isolation as not to degrade the $^{138}\mathrm{Ba}^+$ state detection, cooling, or coherent operations. The relatively similar masses of barium and ytterbium and the small ratio of radial to axial confinement in the trap enable significant coupling between the radial modes of the different species [39], which in turn allows for efficient sympathetic cooling.

With continuous sympathetic cooling, we are able to perform entanglement attempts without stopping for recooling, recovering our full attempt rate of 1 MHz. Although our hardware counter resets at $2^{14} = 16384$ attempts, we estimate a success probability of $2.50(8) \times 10^{-4}$ when allowing a maximum of $N = 20,000$ attempts, which is enough to generate a heralding signal $> 99\%$ of the time (see Supplemental Material). This corresponds to an entanglement rate of 250(8) s^{-1}.

This rate surpasses any previous mark in a system with Bell state fidelities above 70% [40]. This is made possible by imaging systems with larger numerical apertures and the introduction of sympathetic cooling during photon-mediated entanglement generation attempts. Dual-species or *omg* [41] operation is already necessary in most trapped-ion computing and networking architectures and has been demonstrated in numerous experiments [16, 20, 25], so sympathetic cooling for this application does not require a uniquely burdensome overhead.

The dominance of imperfect polarization encoding in our error budget suggests that alternative photonic-qubit encodings, such as frequency [42] and time-bin [43, 44], may be beneficial for short and medium-distance networking in addition to their usual application across longer distances [45]. The former could be available using the $^{137}\mathrm{Ba}^+$ or $^{133}\mathrm{Ba}^+$ isotopes while the latter benefits from the long D state lifetimes in any barium isotope.

Our rate of entanglement generation could be improved by almost a factor of three by replacing AOMs with electro-optic control to reduce latency. Building a duplicate of this system and using both imaging systems of each chamber to collect light from a single ion would again double the success probability reported here, providing a road map to kHz-level remote entanglement rates between atomic memories. Further increases could be achieved using Purcell enhancement in short optical cavities or large-scale spatial multiplexing with integrated optics [46].

This work is supported by the DOE Quantum Systems Accelerator (DE-FOA-0002253) and the NSF STAQ Program (PHY-1818914). J.O. is supported by the National Science Foundation Graduate Research Fellowship (DGE 2139754).

[1] L.-M. Duan and C. Monroe, Rev. Mod. Phys. **82**, 1209 (2010).

[2] H. Bernien, B. Hensen, W. Pfaff, G. Koolstra, M. S. Blok, L. Robledo, T. H. Taminiau, M. Markham, D. J. Twitchen, L. Childress, and R. Hanson, Nature **497**, 86 (2013).

[3] C. J. Axline, L. D. Burkhart, W. Pfaff, M. Zhang, K. Chou, P. Campagne-Ibarcq, P. Reinhold, L. Frunzio, S. M. Girvin, L. Jiang, M. H. Devoret, and R. J. Schoelkopf, Nature Physics **14**, 705 (2018).

[4] C. B. Young, A. Safari, P. Huft, J. Zhang, E. Oh, R. Chinnarasu, and M. Saffman, Applied Physics B: Lasers and Optics **128** (2022), 10.1007/s00340-022-07865-0.

[5] D. Gottesman and I. L. Chuang, Nature **402**, 390 (1999).

[6] L. Jiang, J. M. Taylor, A. S. Sørensen, and M. D. Lukin, Physical Review A - Atomic, Molecular, and Optical Physics **76**, 1 (2007).

[7] C. Monroe, R. Raussendorf, A. Ruthven, K. R. Brown, P. Maunz, L. M. Duan, and J. Kim, Physical Review A - Atomic, Molecular, and Optical Physics **89**, 1 (2014).

[8] P. Komar, E. M. Kessler, M. Bishof, L. Jiang, A. S. Sørensen, J. Ye, and M. D. Lukin, Nature Physics **10**, 582 (2014).

[9] B. C. Nichol, R. Srinivas, D. P. Nadlinger, P. Drmota, D. Main, G. Araneda, C. J. Ballance, and D. M. Lucas, Nature **609**, 689 (2022).

[10] D. P. Nadlinger, P. Drmota, B. C. Nichol, G. Araneda, D. Main, R. Srinivas, D. M. Lucas, C. J. Ballance, K. Ivanov, E. Y. Tan, P. Sekatski, R. L. Urbanke, R. Renner, N. Sangouard, and J. D. Bancal, Nature **607** (2022), 10.1038/s41586-022-04941-5.

[11] C. D. Bruzewicz, J. Chiaverini, R. McConnell, and J. M. Sage, Applied Physics Reviews **6** (2019), 10.1063/1.5088164.

[12] A. Ransford, C. Roman, T. Dellaert, P. McMillin, and W. C. Campbell, Physical Review A **104** (2021), 10.1103/PhysRevA.104.L060402.

[13] C. J. Ballance, T. P. Harty, N. M. Linke, M. A. Sepiol, and D. M. Lucas, Physical Review Letters **117** (2016), 10.1103/PhysRevLett.117.060504.

[14] R. Srinivas, S. C. Burd, H. M. Knaack, R. T. Sutherland, A. Kwiatkowski, S. Glancy, E. Knill, D. J.

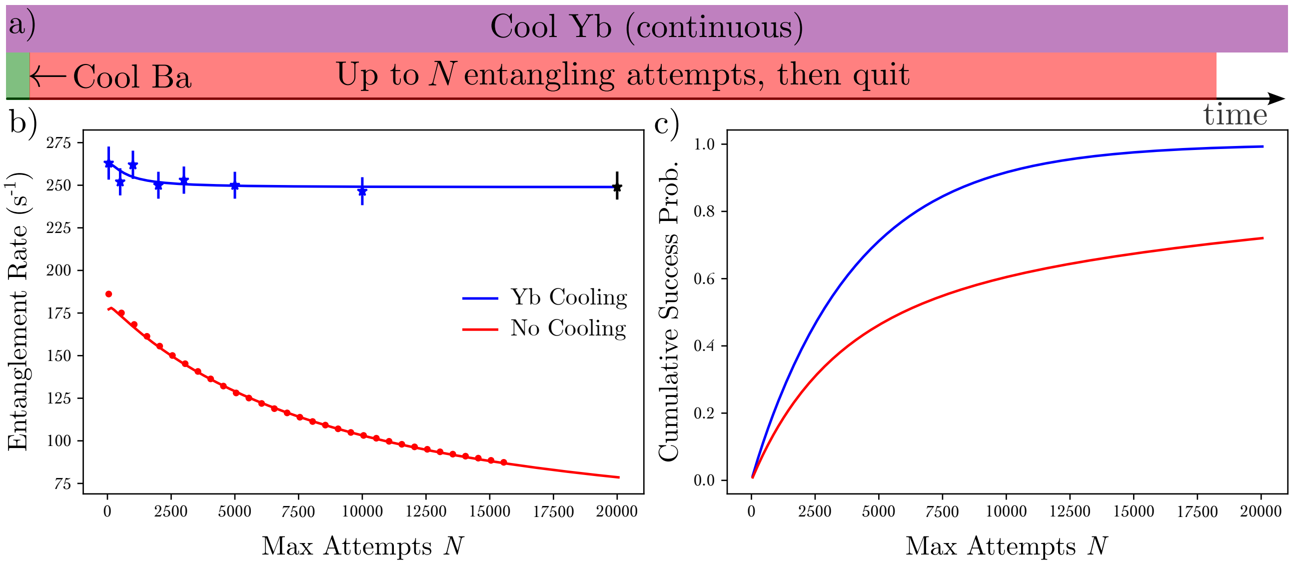

Figure 4. (a) New experimental sequence with an ytterbium sympathetic coolant present in the Coulomb crystal. Instead of repeating the cooling-attempt loop cycle until we herald entanglement, for each requested event we initialize by Doppler cooling the barium ion for 100 μs and then execute attempts until we either succeed or reach N failures. Meanwhile, we continuously Doppler cool the ytterbium ion. (b) Average entanglement rate for different maximum attempt loop lengths with (blue) and without (red) the ytterbium sympathetic coolant. For a more direct comparison, we ignore recooling time in the no-Yb case. The final, black point is based on a fit to the blue data. (c) Cumulative probability to get a successful herald at some point during an attempt loop of up to length N for the inferred probability distributions of the Yb-cooling and no-cooling runs in (b).

Wineland, D. Leibfried, A. C. Wilson, D. T. Allcock, and D. H. Slichter, Nature **597**, 209 (2021).

[15] C. R. Clark, H. N. Tinkey, B. C. Sawyer, A. M. Meier, K. A. Burkhardt, C. M. Seck, C. M. Shappert, N. D. Guise, C. E. Volin, S. D. Fallek, H. T. Hayden, W. G. Rellergert, and K. R. Brown, Physical Review Letters **127**, 130505 (2021).

[16] M. Cetina, L. N. Egan, C. Noel, M. L. Goldman, D. Biswas, A. R. Risinger, D. Zhu, and C. Monroe, PRX Quantum **3** (2022), 10.1103/PRXQuantum.3.010334.

[17] J.-S. Chen, E. Nielsen, M. Ebert, V. Inlek, K. Wright, V. Chaplin, A. Maksymov, E. Páez, A. Poudel, P. Maunz, and J. Gamble, arXiv 2308.05071 (2023).

[18] D. Kielpinski, C. Monroe, and D. J. Wineland, Nature **417**, 709 (2002).

[19] J. M. Pino, J. M. Dreiling, C. Figgatt, J. P. Gaebler, S. A. Moses, M. S. Allman, C. H. Baldwin, M. Foss-Feig, D. Hayes, K. Mayer, C. Ryan-Anderson, and B. Neyenhuis, Nature **592**, 209 (2021).

[20] S. A. Moses *et al.*, Phys. Rev. X **13**, 041052 (2023).

[21] L. J. Stephenson, D. P. Nadlinger, B. C. Nichol, S. An, P. Drmota, T. G. Ballance, K. Thirumalai, J. F. Goodwin, D. M. Lucas, and C. J. Ballance, Physical Review Letters **124**, 1 (2020).

[22] L. Egan, D. M. Debroy, C. Noel, A. Risinger, D. Zhu, D. Biswas, M. Newman, M. Li, K. R. Brown, M. Cetina, and C. Monroe, Nature **598**, 281 (2021).

[23] L. Postler, F. Butt, I. Pogorelov, C. D. Marciniak, S. Heußen, R. Blatt, P. Schindler, M. Rispler, M. Müller, and T. Monz, arXiv 2312.09745 (2023).

[24] V. Krutyanskiy *et al.*, Physical Review Letters **130** (2023), 10.1103/PhysRevLett.130.050803.

[25] P. Drmota, D. Main, D. P. Nadlinger, B. C. Nichol, M. A. Weber, E. M. Ainley, A. Agrawal, R. Srinivas, G. Araneda, C. J. Ballance, and D. M. Lucas, Physical Review Letters **130** (2023), 10.1103/PhysRevLett.130.090803.

[26] A. L. Carter, J. O'Reilly, G. Toh, S. Saha, M. Shalaev, I. Goetting, and C. Monroe, Review of Scientific Instruments **95**, 033201 (2024), https://pubs.aip.org/aip/rsi/article-pdf/doi/10.1063/5.0180732/19732485/033201_1_5.0180732.pdf.

[27] C. Simon and W. T. Irvine, Physical Review Letters **91**, 1 (2003).

[28] J. Hannegan, U. Saha, J. D. Siverns, J. Cassell, E. Waks, and Q. Quraishi, Applied Physics Letters **119** (2021), 10.1063/5.0059966.

[29] M. R. Dietrich, A. Avril, R. Bowler, N. Kurz, J. S. Salacka, G. Shu, and B. B. Blinov (2009) pp. 25–30.

[30] A. Keselman, Y. Glickman, N. Akerman, S. Kotler, and R. Ozeri, New Journal of Physics **13** (2011), 10.1088/1367-2630/13/7/073027.

[31] C. Crocker, M. Lichtman, K. Sosnova, A. Carter, S. Scarano, and C. Monroe, Optics Express **27**, 28143 (2019).

[32] C. Auchter, C.-K. Chou, T. W. Noel, and B. B. Blinov, Journal of the Optical Society of America B **31**, 1568 (2014).

[33] D. A. Lidar, I. L. Chuang, and K. B. Whaley, "Decoherence-free subspaces for quantum computation," (1998).

[34] T. Monz, K. Kim, A. S. Villar, P. Schindler, M. Chwalla, M. Riebe, C. F. Roos, H. Häffner, W. Hänsel, M. Hennrich, and R. Blatt, Physical Review Letters **103** (2009), 10.1103/PhysRevLett.103.200503.

[35] C. A. Sackett, D. Kielpinski, B. E. King, C. Langer, V. Meyer, C. J. Myatt, M. Rowe, Q. A. Turchette, W. M. Itano, D. J. Wineland, and C. Monroe, Nature **404**, 256 (2000).

[36] L. Slodička, G. Hétet, N. Röck, P. Schindler, M. Hennrich, and R. Blatt, Physical Review Letters **110**, 1 (2013).

[37] B. Casabone, A. Stute, K. Friebe, B. Brandstätter, K. Schüppert, R. Blatt, and T. E. Northup, Physical Review Letters **111** (2013), 10.1103/PhysRevLett.111.100505.

[38] D. Hucul, I. V. Inlek, G. Vittorini, C. Crocker, S. Debnath, S. M. Clark, and C. Monroe, Nature Physics **11**, 37 (2015).

[39] K. Sosnova, A. Carter, and C. Monroe, Physical Review A **103** (2021), 10.1103/PhysRevA.103.012610.

[40] R. Stockill, M. J. Stanley, L. Huthmacher, E. Clarke, M. Hugues, A. J. Miller, C. Matthiesen, C. L. Gall, and M. Atatüre, Physical Review Letters **119** (2017), 10.1103/PhysRevLett.119.010503.

[41] D. T. C. Allcock, W. C. Campbell, J. Chiaverini, I. L. Chuang, E. R. Hudson, I. D. Moore, A. Ransford, C. Roman, J. M. Sage, and D. J. Wineland, Applied Physics Letters **119**, 1 (2021).

[42] P. Maunz, S. Olmschenk, D. Hayes, D. N. Matsukevich, L. M. Duan, and C. Monroe, Physical Review Letters **102** (2009), 10.1103/PhysRevLett.102.250502.

[43] T. Ward and M. Keller, New Journal of Physics **24** (2022), 10.1088/1367-2630/aca9ee.

[44] A. Tchebotareva, S. L. Hermans, P. C. Humphreys, D. Voigt, P. J. Harmsma, L. K. Cheng, A. L. Verlaan, N. Dijkhuizen, W. D. Jong, A. Dréau, and R. Hanson, Physical Review Letters **123** (2019), 10.1103/PhysRevLett.123.063601.

[45] E. Bersin *et al.*, Physical Review Applied **21** (2024), 10.1103/PhysRevApplied.21.014024.

[46] M. Ghadimi, V. Blums, B. G. Norton, P. M. Fisher, S. C. Connell, J. M. Amini, C. Volin, H. Hayden, C. S. Pai, D. Kielpinski, M. Lobino, and E. W. Streed, npj Quantum Information **3**, 4 (2017), arXiv: 1607.00100.

[47] D. D. Munshi, T. Dutta, R. Rebhi, and M. Mukherjee, Physical Review A - Atomic, Molecular, and Optical Physics **91** (2015), 10.1103/PhysRevA.91.040501.

[48] C. Shen and L. M. Duan, New Journal of Physics **14** (2012), 10.1088/1367-2630/14/5/053053.

[49] A. Seif, K. A. Landsman, N. M. Linke, C. Figgatt, C. Monroe, and M. Hafezi, Journal of Physics B: Atomic, Molecular and Optical Physics **51** (2018), 10.1088/1361-6455/aad62b.

[50] D. James, Appl. Phys. B **66**, 181 (1998).

[51] A. Sorensen and K. Molmer, Physical Review A **62** (2000).

[52] F. SchmidtKaler, H. Häffner, M. Riebe, S. Gulde, G. P. Lancaster, T. Deuschle, C. Becher, C. F. Roos, J. Eschner, and R. Blatt, Nature **422**, 408 (2003).

[53] J. P. Home, "Quantum science and metrology with mixed-species ion chains," (Academic Press Inc., 2013) pp. 231–277.

I. SUPPLEMENTAL MATERIAL

A. Pulsed excitation

To produce pulsed 493 nm light, we use a mode-locked Coherent Mira 900P Ti:Sapphire laser at 986 nm and subsequently frequency-double the light using second harmonic generation (SHG) to make 493 nm. The laser generates 3 ps pulses with a repetition rate of 76 MHz. The train of 986 nm pulses enters an electro-optic pulse picker, which transmits single, on-demand pulses with an extinction ratio of about 500:1. After frequency doubling with a MgO-doped, periodically-poled lithium niobate crystal, this extinction ratio increases to 250,000:1. Finally, we send the pulses through an AOM for further extinction and power control before routing them to the vacuum chamber via polarization-maintaining optical fiber.

B. Photon collection efficiencies

In each attempt, we pump to $|\downarrow\rangle$ with 96(2)% fidelity and excite an average of 96(2)% of the population to $|P_{1/2}, m_J = +1/2\rangle$. Based on the branching ratio back to $S_{1/2}$, a 493 nm photon is emitted in 73.2% [47] of decay events. The photons are collected by a 0.8 NA objective that covers 20% of the emission solid angle, but within that area only 97(1)% of the photons make it past the trap rods and the lens has a transmission of 91(3)% [26]. We measure a fiber coupling efficiency of 30(3)% and detect photons with avalanche photo-detectors that have specified quantum efficiencies of 71%. In total, from either imaging system, we expect a single photon detection in 2.5(3)% of trials, which is consistent with our measured values of 2.3(1) and 2.2(1)%. We believe that the measured values are a bit lower due to ion recoil heating and additional photonic losses from polarizers, waveplates, and optical filters.

C. Two-ion state detection

We detect the state of the qubit(s) at the end of an experiment by shelving the $|\downarrow\rangle$ population in the $|D_{5/2}, m_J = -1/2\rangle$ state. We shelve using 1762 nm light produced by a thulium-doped fiber laser and fiber amplifier. This system produces 450 mW of 1762 nm light and is stabilized to < 200 Hz by locking to a high-finesse optical cavity with an ultra-low expansion (ULE) glass spacer. After shelving, we apply all polarizations of 493 and 650 nm light, which causes unshelved ions in $|\uparrow\rangle$ to fluoresce while shelved ions remain dark in the metastable $D_{5/2}$ manifold, see Figure 5(a-b). We collect and detect these fluorescence photons using the imaging system shown in Figure 1 [29, 30].

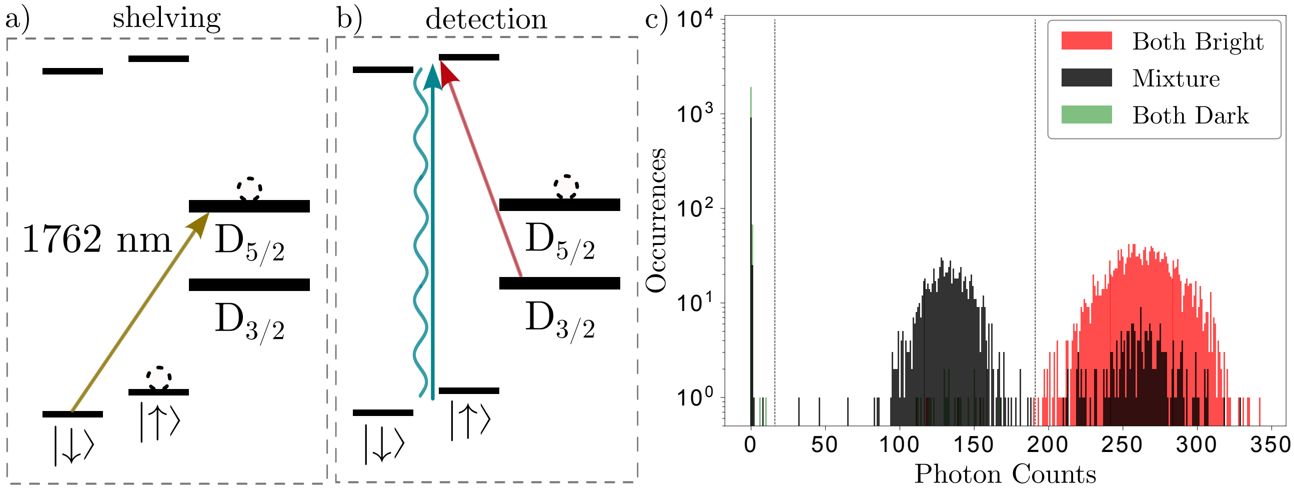

Figure 5. Two-ion state detection. (a) We shelve the $|\downarrow\rangle$ state of each ion to the metastable $D_{5/2}$ manifold. (b) When we subsequently apply 493 and 650 nm light, the shelved population remains dark while any $|\uparrow\rangle$ population fluoresces. (c) We collect 493 nm scattered photons from the ions for 1 ms using the imaging system shown in Figure 1 and set threshold values that separate the photon count distributions for zero, one, or two bright ions with high fidelity. In this example, both bright corresponds to pumping both ions to $|\uparrow\rangle$, both dark corresponds to pumping both to $|\downarrow\rangle$ and shelving, and mixture is the result of applying a partial shelving pulse so that we get significant one-bright population.

Collecting fluorescence for 1 ms provides well-resolved photon number histograms for the cases of no bright ions, one bright ion, and two bright ions, as shown in Figure 5(c). Imperfect shelving reduces the no-bright detection fidelity to 98.7(4)% with erroneous events predominantly registering as one-bright events. The decay of fiber coupling due to heating during experiments reduces the two-bright average fidelity to 98.1(4)%. We correct for these and their corresponding single-ion errors by applying the inverse transformations to the data [48, 49].

D. Ion-ion entanglement fidelity bound

The global nature of our Raman addressing system limits us to analyzing the state fidelity relative to the state

$$|\Psi^+\rangle \equiv \frac{|\downarrow\rangle\,|\uparrow\rangle + |\uparrow\rangle\,|\downarrow\rangle}{\sqrt{2}} \tag{4}$$

because the singlet state $|\Psi^-\rangle$ is invariant under global rotations. We begin this process by measuring the state populations $\rho_{\downarrow\uparrow} + \rho_{\uparrow\downarrow} = 97.6(5)\%$. After waiting 210 μs for $\Delta\omega t = -\Delta\phi$, we apply a global $\frac{\pi}{2}$ rotation that converts $|\Psi^+\rangle$ into $|\Phi^+\rangle = \frac{1}{\sqrt{2}}\left(|\downarrow\downarrow\rangle + |\uparrow\uparrow\rangle\right)$ followed by a second $\frac{\pi}{2}$ pulse with varying phase ϕ. The maximum of the parity $P \equiv \tilde{\rho}_{\downarrow\downarrow} + \tilde{\rho}_{\uparrow\uparrow} - \tilde{\rho}_{\downarrow\uparrow} - \tilde{\rho}_{\uparrow\downarrow}$ of the rotated state in this scan, shown in Figure 3, corresponds to $2\mathrm{Re}\left(\rho_{\downarrow\uparrow,\uparrow\downarrow} + \rho_{\downarrow\downarrow,\uparrow\uparrow}\right) = 92.5(1.7)\%$ [35, 36]. We bound the contribution of the undesired coherence $\rho_{\downarrow\downarrow,\uparrow\uparrow}$ by scanning the phase of a single $\frac{\pi}{2}$ pulse. The only term contributing any contrast to this scan is $2\left[\sin(2\phi)\mathrm{Im}(\rho_{\downarrow\uparrow,\uparrow\downarrow}) - \cos(2\phi)\mathrm{Re}\left(\rho_{\downarrow\uparrow,\uparrow\downarrow}\right)\right] = 2.7(1.8)\%$ [36], so we find $F \geq 93.7(1.3)\%$ [37].

E. Yb-Ba-Ba collective motional modes

Coulomb forces between ions co-trapped in a harmonic potential U lead to collective motional modes that are often used as an information bus for local entangling gates in trapped ion systems [50–52]. In our application, the collective nature allows us to cool the barium ions via their coupling to the ytterbium ion's motion. Using our measured secular frequencies for a single barium ion [26], we can find the structure of the modes in our Yb-Ba-Ba chain by solving

$$\sum_{i,j=1}^{N} \left.\frac{\partial U}{\partial q_i \partial q_j}\right|_0 b_{im} = \omega_m^2 m_i b_{im} \tag{5}$$

where q_i is the position of ion i, ω_m is the secular frequency of mode m, and b_{im} is the participation eigenvector of ion i in mode m with $\sum_i b_{im} b_{in} = \delta_{nm}$ and $\sum_m b_{im} b_{jm} = \delta_{ij}$.

The excitation and pumping beams are delivered at 45° relative to the trap axis and emission is isotropic, so we need to sympathetically cool both the radial and axial directions. Multi-species ion traps often suffer from weak radial coupling between the species [39, 53], but this is circumvented by using a high ratio of axial to radial confinement (see Table I).

	^{171}Yb$^+$	^{138}Ba$^+$	^{138}Ba$^+$	$\omega_m/2\pi$ (kHz)
Axial Mode 1	0.614	0.640	0.300	353
Axial Mode 2	0.567	-0.126	-0.840	604
Axial Mode 3	0.549	-0.758	0.453	872
Radial Mode 1	0.178	0.412	0.847	868
Radial Mode 2	0.587	0.672	-0.512	737
Radial Mode 3	0.790	-0.615	0.144	606

Table I. Collective secular motional mode participation eigenvector matrix b_{im} of the Yb-Ba-Ba Coulomb crystal that we trap for sympathetic cooling experiments. Ions with different charge-to-mass ratios typically have good mutual participation in axial modes, and we also maintain strong coupling in the radial modes thanks to our relatively weak radial confinement [39].

F. Deriving $\bar{p}(N)$

In a system where the probability of success on the n^{th} trial $p(n) \equiv p$ is constant [25], we expect an exponential distribution of required trials n before success each time we attempt to generate entanglement: $\text{PDF}(n) = pe^{-np}$. Instead, we observe a success probability that decays to a steady-state value $p(n) = Ae^{-Bn} + C$ (Fig. 4(b)), stemming from the increased Doppler temperature of the high-intensity optical pumping beam. In this case, we extend the trial number n as a continuous variable and use

$$\text{PDF}(n) = p(n)\left(1 - \int_0^n \text{PDF}(n')\text{d}n'\right) \tag{6}$$

to find

$$\text{PDF}(n) = \exp\left[\frac{A}{B}(e^{-Bn} - 1) - Cn\right](Ae^{-Bn} + C). \tag{7}$$

Integrating this from 0 to N, we find the cumulative density function, or the probability of success up through N trials,

$$\text{CDF}(N) = 1 - \exp\left[\frac{A}{B}(e^{-BN} - 1) - CN\right]. \tag{8}$$

Finally, we arrive at the average success probability by dividing the probability of success up through N trials by the total attempts that have been executed up to the N^{th} in each loop, resulting in

$$\bar{p}(N) = \frac{\text{CDF}(N)}{N + 1 - \int_0^N \text{CDF}(n)\text{d}n}. \tag{9}$$

While we could not find an analytic solution for the integral, we were able to fit the blue data points in Figure 4(c) to this equation by integrating numerically.